Multi-MHz Inductive and Capacitive Power Transfer Systems With PCB-Based Self-Resonators

Yao Wang, *Member, IEEE*, Kaiyuan Wang, *Student Member, IEEE*, Kerui Li, *Member, IEEE*, Yun Yang, *Senior Member, IEEE*, and Shu Yuen Ron Hui, *Fellow, IEEE*

***Abstract*—This article presents multimegahertz (multi-MHz) wireless power transfer technology utilizing integrated printed-circuit-board (PCB) self-resonators, designed for both inductive and capacitive power transfer (IPT and CPT) systems. The PCB resonator comprises a pair of contactless PCB-coil plates incorporating trace inductance and integrated plate capacitance. In IPT systems, the plate capacitances between PCB coils are used to compensate the trace inductances, while the trace inductances are adopted to compensate the plate capacitances in CPT systems. 300 W multi-MHz IPT and CPT systems have been developed using 210 mm × 210 mm circular PCB resonators, showcasing stable output current and voltage across a wide range of load variations. A 3 MHz IPT system is verified to operate with the maximum efficiency of 90.5% over a relatively long distance of 10 cm with strong antimisalignment but poor antiload-variation performance. On the contrary, the CPT systems operating at 3.125 MHz, 4.68 MHz, and 6.78 MHz are demonstrated to operate with the maximum efficiencies of 93.14%, 90.56%, and 83.34% over relatively short distances of 6 mm, 15 mm, and 37 mm, respectively, with strong antiload-variation but poor antimisalignment performance.**

***Index Terms*—Capacitive power transfer (CPT), inductive power transfer (IPT), printed-circuit-board (PCB) based self-resonators.**

I. Introduction

NEAR-FIELD wireless power transfer (WPT) generally refers to inductive power transfer (IPT) based on magnetic fields and capacitive power transfer (CPT) based on electrical fields [1], [2], [3], [4]. IPT technology evolving from the centenary Tesla Coil has been commercialized in portable devices and consumer electronics [5]. As a newly emerging technology, although CPT remains largely unexplored [6], its duality with IPT has inspired researchers to explore advanced system modeling [7], novel design methodologies in compensation circuits [8], [9], [10], and control strategies [11], [12]. By far, CPT technologies have been tried in integrated chips [13], robots [14], electric machines [15], and vehicle charging [16] with power levels ranging from milliwatt to over 3 kW and the frequency spectrums from hundreds of kilohertz to 13.56 MHz [17], [18], [19].

Conventional IPT and CPT systems operating at kilohertz frequencies require external capacitors and inductors to compensate the inductive and capacitive couplers, respectively. As WPT systems evolve towards higher power and frequency [20], compensation circuits using air-core inductors tend to be bulky and challenging to integrate. For high-frequency WPT (i.e., $\geq$1 MHz), not just the external compensation inductors, the external compensation capacitors are also costly and could suffer from parameter drifts. In recent years, hybrid WPT systems have garnered increasing attention [21], [22]. Particularly, in [22], a hybrid WPT system is designed with a coupler that integrates both capacitance and inductance, enhancing compactness. However, additional *LCL* compensation networks are still required. To mitigate the complexity associated with external compensation components and achieve high compactness and integration, self-resonant IPT systems without using any external compensation components have been proposed [23], [24], [25], [26], [27], [28], [29], [30], [31], [32]. The compensation of these inductive self-resonant couplers is achieved through their internal parasitic capacitances.

Printed circuit board (PCB) serves as cost-effective platforms for self-resonators, utilizing printed copper traces as inductors and the stray capacitances among the traces for compensation [28], [29], [30], [31], [32]. The main advantages of PCB-based resonators include i) high compactness and integration, ii) lightweight design, iii) ease of mass production, and iv) cost-effectiveness. According to the literature, PCB self-resonators can be classified into two types. In the conventional design, depicted in Fig. 1(a), copper traces are printed on both sides of the PCB base and connected in series by via holes [28], [29], [30], [31]. This configuration forms with the PCB base material, typically FR-4, serving as dielectric for the parasitic capacitance. The improved design, as shown in Fig. 1(b), is recently introduced in [32]. This new PCB resonator design replaces the dielectric medium for parasitic capacitance from FR-4 to air by modifying the resonator structure from Fig. 1(a) to that shown in Fig. 1(b). This enhancement improves the *Q* factor by approximately 4.3 times. Meanwhile, the two PCB boards

Manuscript received 23 April 2024; revised 2 July 2024; accepted 17 July 2024. Date of publication 19 July 2024; date of current version 4 September 2024. This work was supported in part by A∗Star MTC Young Individual Research Grant under Grant M23M7c0115, in part by the Ministry of Education Academic Research Fund Tier-1 under Grant RG134/23, and in part by the Hong Kong RGC Theme-based Research Project under Grant T23-708/24-N. Recommended for publication by Associate Editor C.-S. Lam. *(Corresponding author: Yun Yang.)*

Yao Wang, Kaiyuan Wang, and Yun Yang are with the Nanyang Technological University, Singapore 639673 (e-mail: yao.wang@ntu.edu.sg; kaiyuan002@e.ntu.edu.sg; yun.yang@ntu.edu.sg).

Kerui Li is with the University of Hong Kong, Hong Kong (e-mail: krli@connect.hku.hk).

Shu Yuen Ron Hui is with University of Hong Kong, Hong Kong, and also with the Imperial College London, WC2R 2LS London, U.K. (e-mail: ronhui@eee.hku.hk).

Color versions of one or more figures in this article are available at https://doi.org/10.1109/TPEL.2024.3431226.

Digital Object Identifier 10.1109/TPEL.2024.3431226

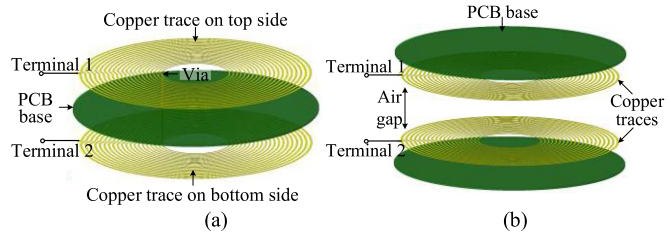

Fig. 1. PCB-based self-resonators based on (a) conventional design and (b) improved design.

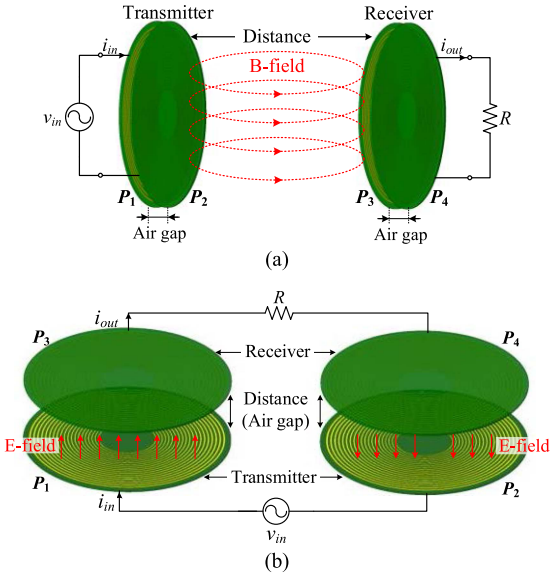

Fig. 2. Structure of the self-resonant (a) IPT and (b) CPT systems without external compensation components.

are noncontact, forming a series resonant network. Li et al. [32] offered valuable insights into the design and optimization of the new PCB self-resonator for achieving a high Q factor. However, the detailed analysis of the working principle of the WPT system is lacking. The reference only demonstrates power transfer using the inductive approach at a low power level of approximately 10 W, which does not fully showcase the potential of PCB resonators.

This study follows up on the research presented in [32]. It contributes in two main aspects.

1) First, this article pioneers the use of these self-resonators for CPT [as depicted in Fig. 2(b)], marking a breakthrough in PCB-based CPT for high-frequency applications. The CPT resonators retain the advantages of adjustable resonant frequencies by varying the distances between the two PCBs (i.e., P_1 and P_3, P_2, and P_4), while fundamentally shifting the power transfer mechanism from magnetic fields to electric fields.
2) Second, this article comprehensively investigates the operational principles and efficiency performance of an IPT system using the enhanced PCB resonator [as depicted in Fig. 2(a)]. The Q factors of the PCB resonators are significantly boosted by employing polytetrafluoroethylene (PTFE) materials, surpassing the previous designs using FR4 materials.

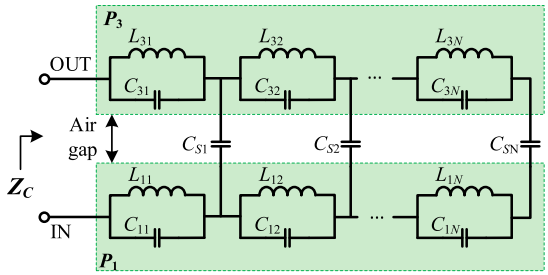

Fig. 3. Equivalent circuit model of the PCB coupler.

To validate the effectiveness of the PCB-based resonators for WPT, four 210 mm $\times$ 210 mm circular PCB-based resonators with PTFE materials are fabricated. A 300 W IPT system utilizing PCB-based resonators has been implemented. The IPT system achieves a maximum efficiency of 90.5% at a frequency of 3 MHz and a transfer distance of 10 cm. Additionally, a 300 W PCB-based CPT system has been developed, achieving maximum efficiencies of 93.14%, 90.56%, and 83.34% at transfer distances of 6 mm, 15 mm, and 37 mm, respectively. The corresponding resonant frequencies are 3.125 MHz, 4.68 MHz, and 6.78 MHz. The PCB-based resonators can be interchangeably used for both IPT and CPT systems without altering the external circuit connections.

II. Analysis of the Self-Resonant PCB Coupler

A. Modeling of the PCB-Based Coupler

Considering the self-inductances of the copper traces, stray capacitances between the coil turns, and the stray capacitances between the PCBs, the equivalent circuit of the PCB coupler [i.e., P_1 and P_3 in Fig. 2(b)] can be modeled, as shown in Fig. 3. Here, $L_{11}, L_{12}, \ldots, L_{1N}$ represent the self-inductance of each turn of the coil in the PCB board P_1. $L_{31}, L_{32}, \ldots, L_{3N}$ represent the self-inductance of each turn of the coil in the PCB board P_3. $C_{11}, C_{12}, \ldots, C_{1N}$ and $C_{31}, C_{32}, \ldots, C_{3N}$ represent the stray capacitances between adjacent coil turns. $C_{S1}, C_{S2}, \ldots, C_{SN}$ represent the coupling capacitances between the two boards. This circuit model applies to both IPT and CPT resonators.

The measured impedance curve of the PCB coupler within a frequency spectrum from 100 kHz to 40 MHz by an impedance analyzer is plotted, as shown in Fig. 4. Obviously, multiple series self-resonant frequencies (i.e., f_s, f_{s1}, f_{s2}, and f_{s3}) and parallel self-resonant frequencies (i.e., f_p and f_{p1}) can be observed from the curve. In this article, both the IPT and CPT systems are designed to operate at their respective first series self-resonant frequencies f_s. This choice simplifies the equivalent circuit models and reduces challenges in designing the inverter and rectifier. To simplify the modeling and analysis of the PCB resonator, only the first series (i.e., f_s) and parallel (i.e., f_p) self-resonant frequencies are considered. A simplified LCR model of the PCB coupler is depicted, as shown in Fig. 5(a). Here, L and r are the equivalent inductance and parasitic resistance of the coupler. C_p

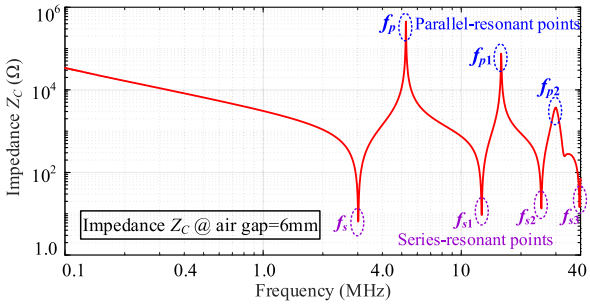

Fig. 4. Impedance response of the PCB coil-based coupler across frequency.

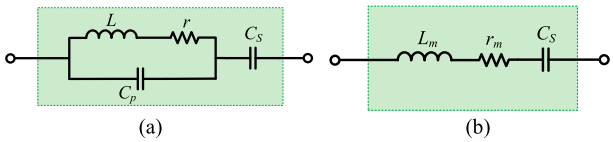

Fig. 5. (a) simplified circuit model of the PCB coupler with consideration of f_s and f_p, and (b) its equivalent series model.

is the equivalent parallel capacitance between the coil turns. C_s is the main series coupling capacitance between the two PCBs.

Based on the circuit in Fig. 5(a), the self-resonant frequencies f_s and f_p satisfy the relationship

$$f_s = \frac{1}{2\pi\sqrt{L\left(C_s + C_p\right)}} \tag{1.1}$$

$$f_p = \frac{1}{2\pi\sqrt{LC_p}} \tag{1.2}$$

The total impedance (i.e., Z_C) can be derived as the expression shown in (2) shown at the bottom of this page, where ω is the angular frequency. L_m and r_m are the equivalent inductance and resistance of the parallel network of L, r, and C_p. To simplify the expressions of L_m and r_m in Fig. 5(b), self-resonant angular frequencies ω_s and ω_p, and the Q factor are defined as

$$\omega_s = \frac{1}{\sqrt{L\left(C_p + C_s\right)}} \tag{3.1}$$

$$\omega_p = \frac{1}{\sqrt{LC_p}} \tag{3.2}$$

$$Q_s = \frac{\omega_s L}{r}. \tag{3.3}$$

Based on (2) and (3), L_m and r_m at the self-resonant angular frequency ω_s can be derived as

$$L_m\left(\omega_s\right) = L\frac{\left(1 - \omega_s^2 LC_p - \frac{C_p}{L}r^2\right)}{\left(1 - \omega_s^2 LC_p\right)^2 + \left(\omega_s C_p r\right)^2}$$

$$= L\frac{1 - \left(\frac{1}{Q_s^2} + 1\right)\frac{\omega_s^2}{\omega_p^2}}{\left(1 - \frac{\omega_s^2}{\omega_p^2}\right)^2 + \left(\frac{1}{Q_s}\cdot\frac{\omega_s^2}{\omega_p^2}\right)^2} \tag{4.1}$$

$$r_m\left(\omega_s\right) = \frac{r}{\left(1 - \omega_s^2 LC_p\right)^2 + \left(\omega_s C_p r\right)^2}$$

$$= \frac{r}{\left(1 - \frac{\omega_s^2}{\omega_p^2}\right)^2 + \left(\frac{1}{Q_s}\cdot\frac{\omega_s^2}{\omega_p^2}\right)^2}. \tag{4.2}$$

It is worth noting that Q_s is generally greater than 10 at self-resonant frequency f_s. Then, (4.1) and (4.2) can be simplified as

$$L_m\left(\omega_s\right) \approx \frac{L}{1 - \frac{\omega_s^2}{\omega_p^2}} = L\left(1 + \frac{C_p}{C_s}\right) \tag{5.1}$$

$$r_m\left(\omega_s\right) \approx \frac{r}{\left(1 - \frac{\omega_s^2}{\omega_p^2}\right)^2} = r\left(1 + \frac{C_p}{C_s}\right)^2. \tag{5.2}$$

The equivalent impedance Z_C at f_s can also be simplified as

$$Z_C\left(\omega_s\right) = r_m. \tag{6}$$

B. Identification of the Main Electrical Parameters

To identify the electrical parameters of the simplified circuit model in Fig. 5(a), an impedance analyzer is adopted to measure the parameters f_s, f_p, and r_m at the high-frequency f_s, while calibrating the parameter C_s at a low frequency (i.e., 10 kHz). Then, the parallel capacitance C_p can be identified based on (1.1) and (1.2) using

$$C_p = \frac{C_s}{\frac{f_p^2}{f_s^2} - 1}. \tag{7}$$

Inductance L can be estimated based on (1.2) and (7) using

$$L = \frac{1}{\omega_p^2 C_p}. \tag{8}$$

The resistance r of the PCB coupler can be estimated based on (5.2) using

$$r = r_m\left(1 - \frac{f_s^2}{f_p^2}\right).^2 \tag{9}$$

The Q factor Q_s of the resonator can be further calculated using (9) and (3.3). The flowchart of the proposed method for determining the parameters C_s, L, r, C_p, and Q_s in Fig. 5(a), is shown in Fig. 6.

To validate the accuracy of the simplified circuit model for the PCB resonator and the effectiveness of the proposed parameter identification method, the calculated impedance from the simplified circuit model based on the identified parameters is compared

$$Z_C\left(\omega\right) = \frac{1}{j\omega C_s} + \omega L\cdot\frac{\left(1 - \omega^2 LC_p - \frac{C_p}{L}r^2\right)}{\left(1 - \omega^2 LC_p\right)^2 + \left(\omega C_p r\right)^2} + \frac{r}{\left(1 - \omega^2 LC_p\right)^2 + \left(\omega C_p r\right)^2} = \frac{1}{j\omega C_s} + j\omega L_m + r_m. \tag{2}$$

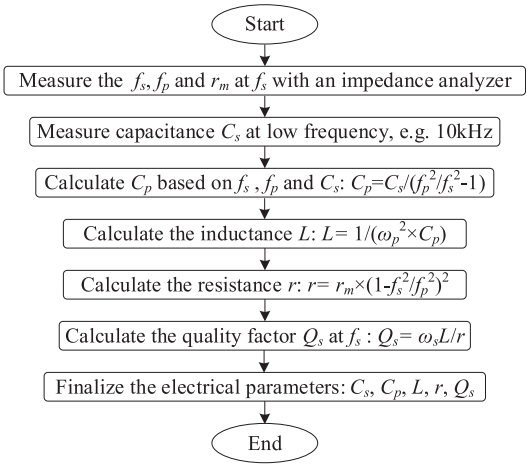

Fig. 6. Flowchat of the algorithm to determine the parameters of the simplified model.

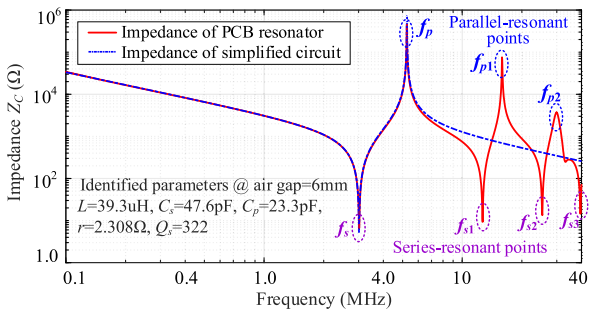

Fig. 7. Comparison between the measured and calculated impedances based on the identified parameters.

with the measured impedance Z_C of the PCB resonator with an impedance analyzer, as shown in Fig. 7.

The results indicate that for operating frequencies below f_p, the measured impedance curves of the PCB resonator align closely with the calculated impedance from the simplified circuit model. This alignment showcases that the simplified circuit model effectively represents the PCB resonator, and the identified parameters are accurate within this frequency range. However, the impedance curves of the PCB resonator and the simplified circuit diverge as the frequency exceeds f_p, indicating that the simplified circuit model loses accuracy in high-frequency spectrum. In this article, both IPT and CPT systems are designed to operate at the first series self-resonant frequency f_s ($f_s < f_p$). Therefore, the proposed simplified circuit remains effective for modeling the IPT and CPT systems at their operating frequencies.

C. Evaluation of the PCB-Based Coupler

The photographs of a fabricated PCB-based self-resonator with PTFE materials are shown in Fig. 8. The front view in Fig. 8(a) shows the diameter of the PCB base (i.e., D_{PCB}), the diameter of the innermost coil (i.e., D_{in}), and the diameter of the outermost coil (i.e., D_{out}). The side view in Fig. 8(b) shows

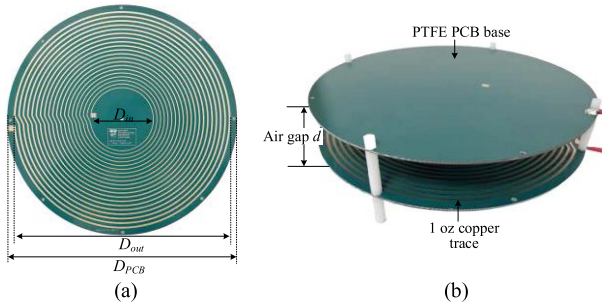

Fig. 8. (a) Front and (b) side views of the PCB-based coupler.

TABLE I
MAIN SPECIFICATIONS OF THE PCB-BASED COUPLER

Parameter	Value
Diameter of PCB D_{PCB}	210 mm
Diameter of innermost coil D_{in}	60 mm
Diameter of Outermost coil D_{out}	200 mm
Coil pitch	2.482 mm
Coil width of the innermost turn	0.794 mm
Coil width of the outermost turn	1.626 mm
Number of coil turns	20
Material of PCB base	Polytetrafluoroethylene (PTFE)
Thickness of PCB base	1.56 mm
Thickness of copper trace	1oz (35 μm)

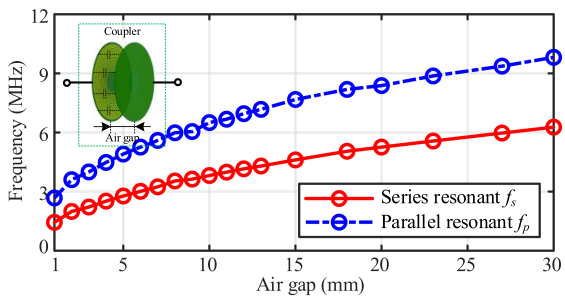

Fig. 9. Self-resonant frequencies f_s and f_p of the resaontor with varying air gaps.

the air gap between the two PCBs (i.e., d). The 1oz spiral copper trace is printed on a PCB base with decreasing coil widths of 1.626 mm and 0.794 mm in the outermost and innermost turns. A coil pitch of 2.482 mm is achieved between adjacent turns. The main specifications of the practical PCB-based coupler are provided in Table I.

By scanning the frequencies of PCB-based resonators, the first series and parallel self-resonant frequencies f_s and f_p can be determined from the impedance curves acquired by the Vector Network Analyzer Bode100. Fig. 9 shows the measured f_s and f_p of the resonator with 19 different air gaps between the two PCBs. Both f_s and f_p are enhanced when the air gaps are increased from 1 mm to 30 mm.

Based on the parameter identification method in Fig. 6, the parameters C_s, C_p, L, r, and Q_s of the simplified circuit in Fig. 5(a) can be determined. Fig. 10 illustrates the variation of capacitances C_p and C_s, which decrease as the air gaps increase.

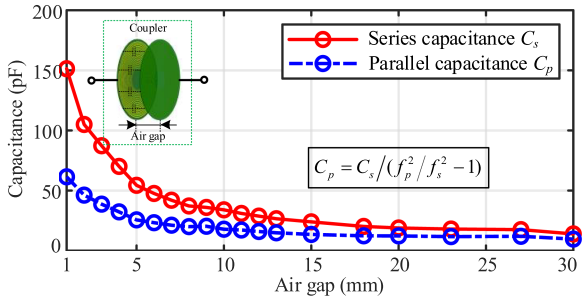

Fig. 10. Parasitic capacitances C_s and C_p of the resonator with varying air gaps.

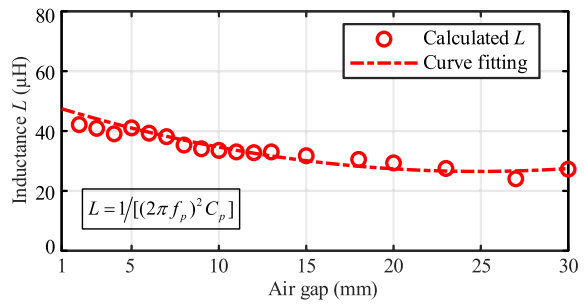

Fig. 11. Calculated inductance L of the resonator with varying air gaps.

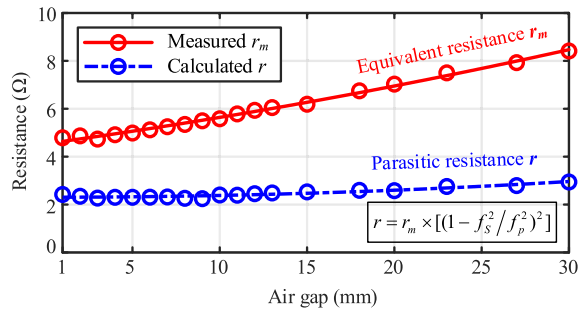

Fig. 12. Parasitic resistances r_m and r of the resonator with varying air gaps.

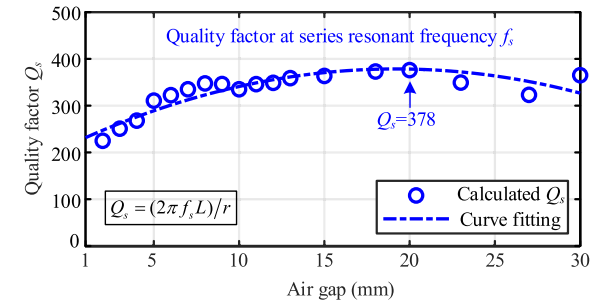

Fig. 13. Quality factors Q_s of the resonator at f_s with varying air gaps.

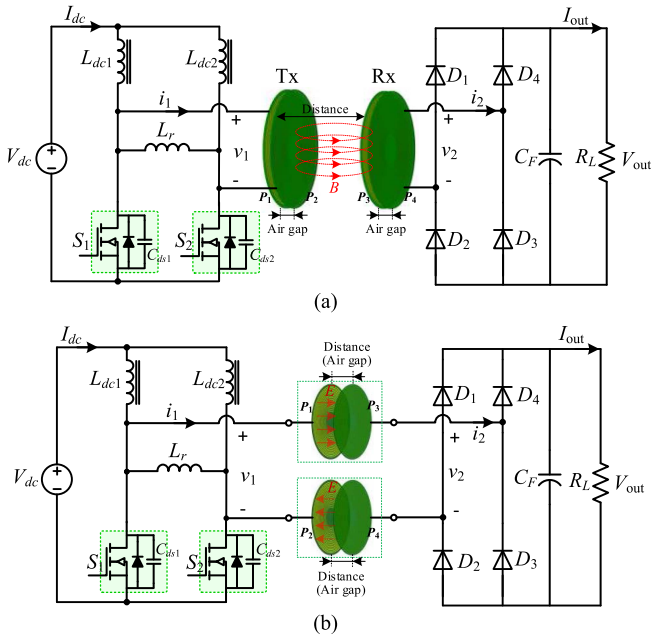

Fig. 14. Circuit topologies of the (a) IPT and (b) CPT systems with the self-resonant PCB couplers.

The inductance L versus air gap is depicted in Fig. 11, showing a gradual reduction as the air gaps increase due to weaker magnetic coupling between the two PCBs. Fig. 12 presents the parasitic resistances r and r_m. Notably, as the air gap increases from 1 mm to 30 mm, the resistance r of the simplified circuit model in Fig. 5(a) remains relatively constant around 2.46 Ω. The corresponding Q_s values of the resonator operating at f_s are provided in Fig. 13, showing all Q_s values are above 200, with the highest Q_s reaching 378 at an air gap of 20 mm.

III. Analysis of the IPT and CPT Systems

A. Circuitry of IPT and CPT Systems With the PCB Coupler

The main circuit topologies of the self-resonant IPT and CPT systems with the PCB couplers are depicted, as shown in Fig. 14. In the IPT coupler, the PCB resonators maintain a fixed air gap, and power is transferred over the distance between these resonators. In contrast, in the CPT coupler, the power transfer distance is equivalent to the air gap of the PCB resonators. Due to the presence of multiple resonant frequencies in practical PCB resonators, they exhibit poor harmonics filtering performance. Therefore, a quasi-sine ac source is implemented using a half-bridge current source inverter to minimize harmonics in the excitation voltage v_1. In contrast to the conventional single-switch Class-E power amplifier, the adopted inverter generates a quasi-sine waveform with reduced harmonics and facilitates higher power conversion. At high sides of the inverter, two dc choke inductors $L_{\rm dc1}$ and $L_{\rm dc2}$ are used to facilitate the high-frequency operations without setting dead times for the power switches S_1 and S_2 at low sides. The inductor L_r is designed to resonate with the parasitic capacitances C_{ds1} and C_{ds2} of the power switches to generate v_1 with small harmonic distortations. Passive diode-bridge rectifiers (i.e., D_1–D_4) are implemented at the receiver sides to achieve dc output. R_L is the load resistance.

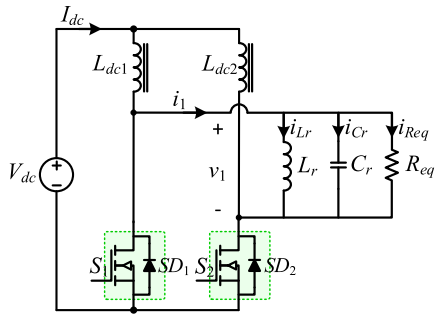

Fig. 15. Equivalent circuit of the half-bridge current source inverter.

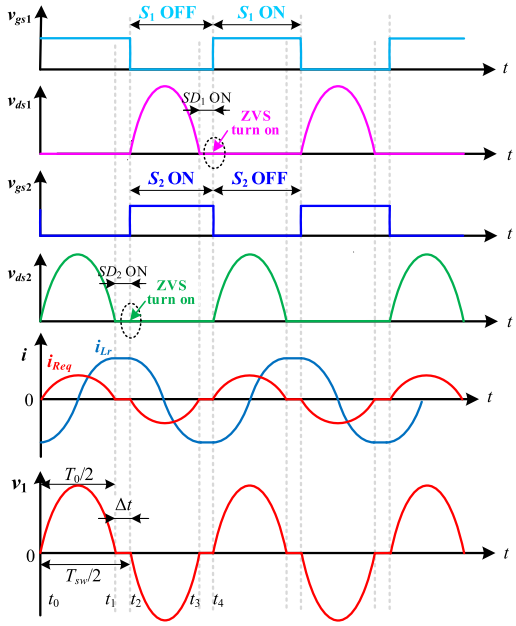

Fig. 16. Schematic waveforms of the main components in the equivalent circuit.

B. Quasi-Sine Inverter With Zero Voltage Switching (ZVS)

The equivalent working circuit of the designed inverter is provided in Fig. 15. C_r is the equivalent resonant capacitor of C_{ds1} and C_{ds2} (i.e., $C_r = C_{ds1} = C_{ds2}$). $R_{\rm eq}$ is the equivalent resistor of the well-compensated WPT system with a resistive load. To achieve ZVS of S_1 and S_2, the resonant frequency of L_r and C_r (i.e., f_0) is designed to be larger than the switching frequency of S_1 and S_2 (i.e., f_{sw}) as

$$f_0 = \frac{1}{2\pi\sqrt{L_r C_r}} > f_{sw}. \tag{10}$$

The schematic waveforms of the gate-to-source voltages (i.e., v_{gs1} and v_{gs2}) and drain-to-source voltages (i.e., v_{ds1} and v_{ds2}) of S_1 and S_2, currents flowing through the inductor L_r and the equivalent load $R_{\rm eq}$ (i.e., i_{Lr} and i_{Req}), and the input ac voltage of the coupler (i.e., v_1) are provided in Fig. 16. When $f_0 > f_{sw}$, v_{ds1}, and v_{ds2} reach zero before the power switches are turned ON, such that ZVS can be achieved. As depicted in Fig. 16, because the time duration Δt for on-state body diodes SD_1 and SD_2 is typically much shorter than the switching period T_{sw}, the waveforms of v_1 closely approximate a sine wave. The expressions of v_1 during one switching period are

$$v_1(t) = \begin{cases} V_0 \sin\left[\omega_0 (t - t_0)\right] & t_0 \le t \le t_1 \\ 0 & t_1 < t < t_2 \\ -V_0 \sin\left[\omega_0 (t - t_2)\right] & t_2 \le t \le t_3 \\ 0 & t_3 < t < t_4 \end{cases} \tag{11.1}$$

where $\omega_0 = 2\pi f_0$, and V_0 is the peak value of $v_1(t)$

$$V_0 = \frac{\pi f_0}{f_{sw}} V_{\rm dc} \tag{11.2}$$

$$t_1 - t_0 = \frac{T_0}{2} = \frac{1}{2f_0} \tag{11.3}$$

$$t_2 - t_0 = \frac{T_{sw}}{2} = \frac{1}{2f_{sw}}. \tag{11.4}$$

The root-mean-square (rms) value of v_1 is

$$V_1\ ({\rm rms}) = \frac{\pi}{\sqrt{2}} \sqrt{\frac{f_0}{f_{sw}}} V_{\rm dc} \approx 2.22 \sqrt{\frac{f_0}{f_{sw}}} V_{\rm dc}. \tag{12}$$

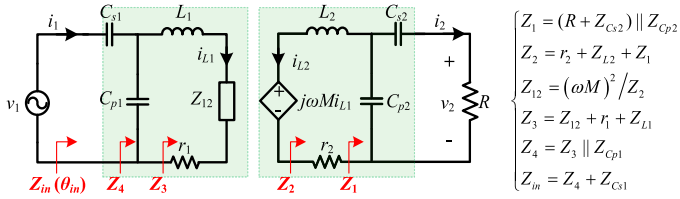

Fig. 17. Equivalent circuit diagram of the self-resonant IPT system.

C. Analysis of the IPT System With the Self-Resonant PCBs

The equivalent circuit of the IPT system with the self-resonant PCB couplers is depicted, as shown in Fig. 17. To simplify the analysis of IPT resonators without losing generality, the main parameters of PCBs are identical as

$$\begin{cases} L_1 = L_2 = L \\ r_1 = r_2 = r \\ C_{p1} = C_{p2} = C_p \\ C_{s1} = C_{s2} = C_s. \end{cases} \tag{13}$$

The mutual inductance M and coupling coefficient k are defined such that

$$M = k\sqrt{L_1 L_2}. \tag{14.1}$$

Then, based on the equivalent impedances and the equivalent circuit shown in Fig. 17, the load current i_2 can be derived as

$$i_2 = \frac{j\omega M Z_1 Z_4 v_1}{Z_{\rm in} Z_3^2 (Z_{Cs2} + R)} \tag{14.2}$$

where R is the equivalent ac load resistance of the nonlinear load. For the investigated systems with negligible parasitic capacitances [33] and moderate load conditions [34], the relationship between the ac resistance R and the dc resistance $R_{\rm L}$ can be

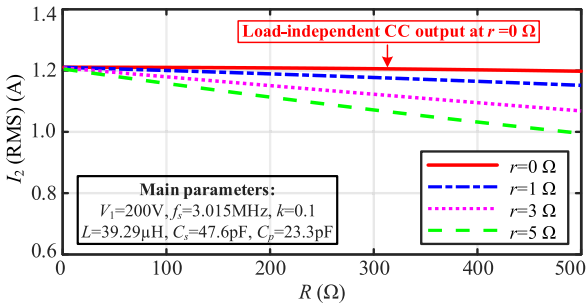

Fig. 18. Curves of I_2(rms) versus R of the IPT system with different r.

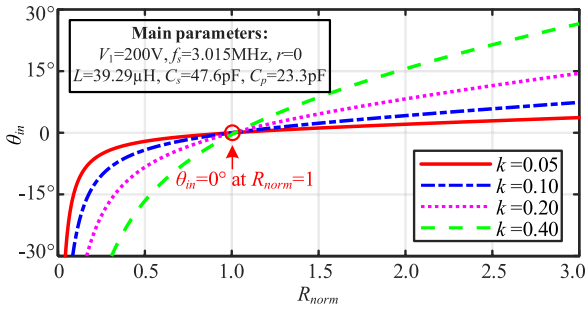

Fig. 19. Phase angle $\theta_{\rm in}$ of $Z_{\rm in}$ at different coupling and load conditions.

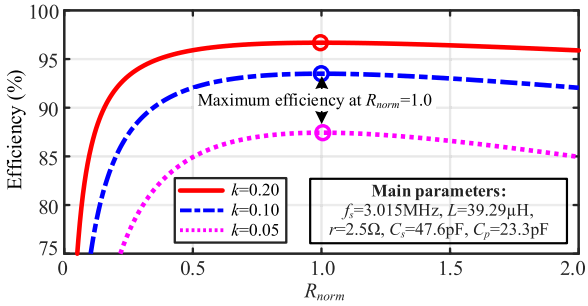

Fig. 20. IPT system efficiencies versus $R_{\rm norm}$ at different coupling conditions.

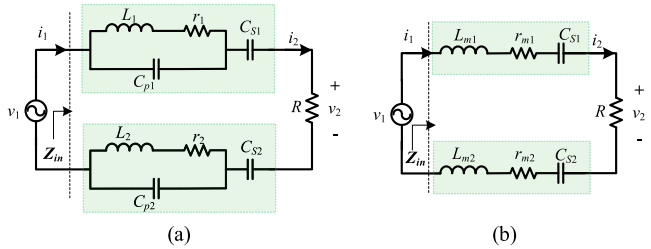

Fig. 21. (a) Equivalent circuit and (b) equivalent simplified circuit of the CPT system with the self-resonant PCB couplers.

simply expressed as

$$R = \frac{8}{\pi^2} R_L. \tag{15.1}$$

To further simplify (14.2), the quality factors Q_{RS} and Q_{RP}, which represent the ratios of impedances of C_s and C_p over the load resistance R, are introduced as

$$Q_{RS} = \frac{1}{\omega_s C_s R} \tag{15.2}$$

$$Q_{RP} = \frac{1}{\omega_s C_p R}. \tag{15.3}$$

For ideal IPT systems (i.e., $r = 0$) with Q_{RS} and Q_{RP} being greater than 10, the current i_2 in (14.2) can be simplified as

$$i_2 = \frac{v_1}{\omega_s M} \cdot \frac{\frac{1}{(Q_{RS}+Q_{RP})} + j}{\frac{1}{Q_{RP}^2} + \left(1 + \frac{C_p}{C_s}\right)^2} \approx j \frac{v_1}{\omega_s M \left(1 + \frac{C_p}{C_s}\right)^2} \tag{16}$$

which exhibits load-independent system characteristics with constant current (CC) outputs.

Fig. 18 shows the curves of the rms values of i_2 versus the system load resistance R with different values of r. The main parameters of the evaluated system are determined based on the prototype in the experiment, which are also shown in Fig. 17. For an ideal IPT system with $r = 0$, I_2(rms) is almost constant over a wide range of load conditions from 0 Ω to 500 Ω. Meantime, the CC output performance will deteriorate as the parasitic r increases.

Fig. 19 shows the curves of the phase angle of the input impedance $Z_{\rm in}$ (i.e., $\theta_{\rm in}$) versus the normalized load resistance $R_{\rm norm}$ of the IPT system with different coupling coefficients k. $R_{\rm norm}$ is introduced for fair comparisons among the IPT cases with different k, which can be expressed as

$$R_{\rm norm} = \frac{R}{\omega_s M \left(1 + \frac{C_p}{C_s}\right)^2}. \tag{17}$$

In Fig. 19, $\theta_{\rm in}$ is changed from negative to positive values as the load resistance increases, which indicates $Z_{\rm in}$ is transformed from capacitance to inductance. For $R_{\rm norm} = 1$, $\theta_{\rm in}$ of the IPT system is kept at 0° even if the coupling coefficient changes.

The efficiency of the IPT system can be calculated based on

$$\eta_{\rm SR-IPT} = \frac{I_2^2 R}{I_2^2 R + I_{L1}^2 r_1 + I_{L2}^2 r_2} = \frac{1}{1 + \frac{r}{R}\left\{\frac{1}{Q_{RP}^2} + \frac{1}{k^2 Q_s^2}\left[\frac{1}{Q_{RP}^2} + \left(\frac{Q_s}{Q_{RS}} + \frac{R}{r}\frac{Q_{RS}}{Q_s}\right)^2\right] + \left(1 + \frac{C_p}{C_s}\right)^2\right\}}. \tag{18}$$

Fig. 20 shows the efficiency curves versus $R_{\rm norm}$ with varying k. A higher coupling coefficient k contributes to a higher efficiency. The maximum efficiency of the system is achieved at $R_{\rm norm} = 1.0$ regardless of coupling variations.

D. Analysis of the CPT System With the Self-Resonant PCBs

The equivalent circuit of the CPT system with the self-resonant PCB couplers is shown in Fig. 21(a). It can be depicted based on the simplified circuit model in Fig. 5. The equivalent circuit model in Fig. 21(a) can be further simplified into Fig. 21(b). The parameters C_{s1} and C_{s2} are directly measured, while the parameters L_{m1}, L_{m2}, r_{m1}, and r_{m2} are derived based

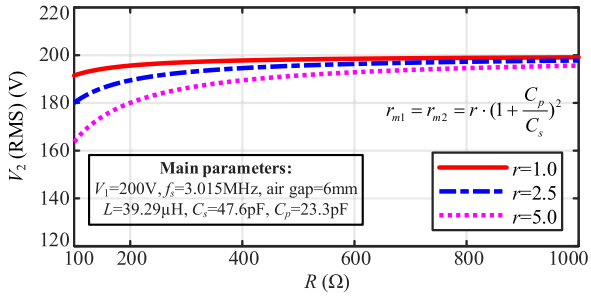

Fig. 22. Rms values of v_2 of the CPT systems at different load conditions.

on (4.1) and (4.2). The input impedance of the CPT system is

$$Z_{\text{in}}|_{\text{CPT}} = R + j\omega\left(L_{m1} + L_{m2}\right) + \frac{1}{j\omega C_{s1}} + \frac{1}{j\omega C_{s2}} + r_{m1} + r_{m2}. \tag{19}$$

When the system operates at f_s, the inductances L_{m1} and L_{m2} are in resonance with C_{s1} and C_{s2}, respectively, to achieve zero phase angle (ZPA). The load resistance R will not affect the resonance, which means the ZPA can be maintained over a wide load range.

When the operating frequency is controlled at the resonant frequency of the LCR circuit in Fig. 21(b), the output voltage v_2 can be derived as

$$v_2 = v_1 \frac{R}{R + r_{m1} + r_{m2}}. \tag{20}$$

If the parasitic resistances r_{m1} and r_{m2} are negligible as compared to load resistance R, the rms value of v_2 can be constant.

To illustrate the output voltage characteristics of the implemented CPT system, the case of a PCB resonator with an air gap of 6 mm (also referred to as the transfer distance) is examined. The voltage characteristics of this configuration are depicted in Fig. 22. The main parameters of the evaluated system are determined based on the prototype used in the experiment, as also shown in Fig. 22. As can be seen from the results, the rms value of v_2 is almost constant with $r = 1$ when $R > 600\ \Omega$.

The efficiency of the CPT system can be calculated based on

$$\eta_{\text{SR-CPT}} = \frac{I_2^2 R}{I_2^2\left(R + r_{m1} + r_{m2}\right)} = \frac{1}{1 + \frac{2r}{R} \cdot \frac{(1+C_p/C_s)^2}{1+1/Q_s^2 \cdot C_p^2/C_s^2}}. \tag{21}$$

Fig. 23(a) shows the efficiency curves of the CPT system with different r and loads. Larger load resistance R and smaller parasitic resistance r contribute to a higher system efficiency. Fig. 23(b) shows the efficiency curves of the CPT system with different C_p/C_s and r. The system efficiency can be improved by decreasing C_p/C_s for a given R and r.

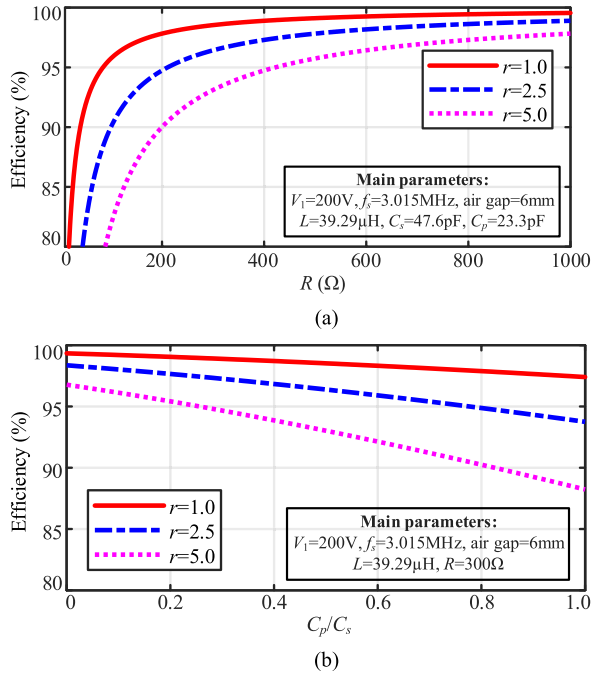

Fig. 23. CPT system efficiencies versus (a) R and (b) C_p/C_s with different r.

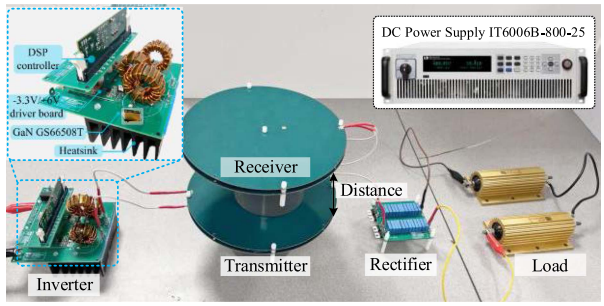

Fig. 24. Photograph of the practical IPT setup.

IV. Experimental Verification of PCB-Based IPT

The photograph of the practical IPT setup is shown in Fig. 24. A quasi-sine ac source is designed based on the half-bridge current-source inverter topology with two gallium nitride (GaN) switches GS66508T. Si8271 is adopted for gate drives. The digital signal processor TMS320F28335 is used to generate control signals. The dc choke inductors are designed based on magnetic rings of fair-rite 67 materials. Full-bridge rectifier is implemented by four silicon carbide (SiC) diodes (i.e., C4D02120A) at the receiver side. The resonant inductor L_r is employed to offset the drain-source capacitance C_{ds} of GaN FET. Given the nonlinearity of C_{ds} with respect to voltage, additional high-frequency C0G capacitors of 200 pF are externally placed across the drain and source terminals of the GaN FET to mitigate this issue. The inductor L_r is constructed using 2-mm copper wire and fair-rite 67 material magnetic rings. Its inductance is adjusted to achieve ZVS operation of the inverter under no-load conditions before integrating it into the IPT system.

In the IPT system, the air gap of PCB resonators is set at 6 mm, resulting in a self-resonant frequency of 3.015 MHz and a Q factor of 322. The inductance L_r is adjusted to 6.7μH to enable ZVS operation of the inverter. Using a dc power supply IT60006B-800-25 to generate a 100 V dc input voltage, the

TABLE II
MAIN PARAMETERS OF COMPONENTS IN THE IPT SYSTEM

Parameter	Value	Parameter	Value
V_{dc}	100 V (dc)	R_L	50 Ω−300 Ω
GaN FET	GS66508T	Diode	C4D02120A
Magnetic ring	fair-rite 67	PCB air gap d_p	6 mm
f_s	3.015MHz	f_p	5.26 MHz
L_1, L_2	39.3μH	C_{s1}, C_{s2}	47.6 pF
r_1, r_2	2.308Ω	C_{p1}, C_{p2}	23.3 pF
Q_1, Q_2	322	L_r	6.7 μH
Transfer distance	100mm/120 mm	k_{max}	0.103/0.075
Misalignment	0−100 mm	k_{min}	0.041/0.034

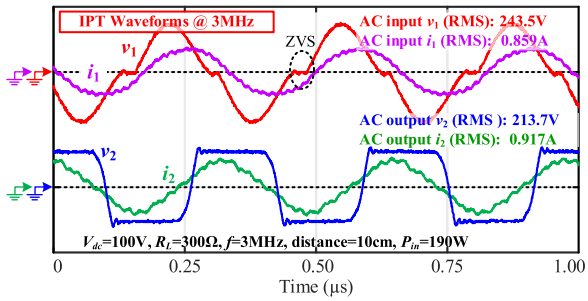

Fig. 25. Input and output voltage and current waveforms of the coupled resonators in the IPT system.

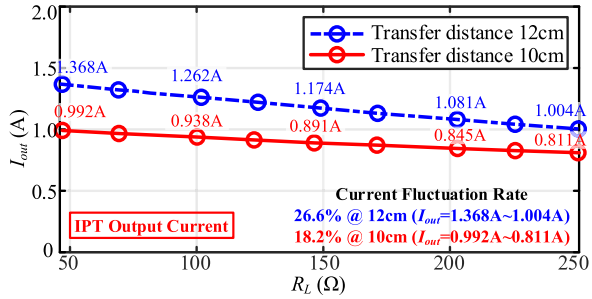

Fig. 26. Output DC currents of the IPT systems with different load conditions and transfer distances.

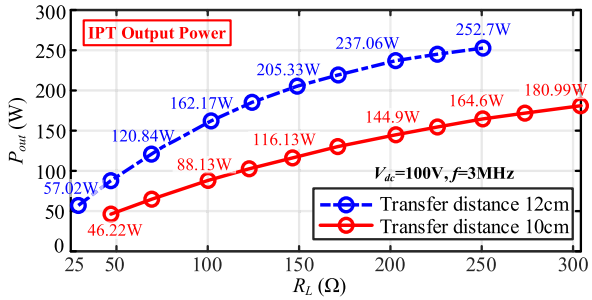

Fig. 27. Output power of the IPT systems with different load conditions and transfer distances.

performance of the IPT system was evaluated at two distinct transfer distances: 100 mm and 120 mm. The evaluation covered a wide load range from 50 Ω to 300 Ω and lateral misalignment varying from 0 to 100 mm. At distances of 100 mm and 120 mm, the coupling coefficient k ranged from 0.103 to 0.041 and from 0.075 to 0.034, respectively. Detailed parameters are provided in Table II.

A. Voltage and Current Waveforms of the Coupled Resonators

Fig. 25 demonstrates the waveforms of input and output voltages and currents in the IPT system with a 100 V dc input voltage, a 10 cm transfer distance, and a 300 Ω load. A quasi-sine input voltage v_1 with the rms value of 243.5 V is achieved, consistent with the theoretical analysis. The input current i_1 slightly lags v_1 in phase, contributing to the ZVS operation of the inverter. The output current i_2 slightly leads the output voltage v_2 in phase, which is attributed to the parasitic capacitances of the rectifier diodes. The ripples observed on the input and output currents mainly stem from the diode-bridge rectifier and the PCB-based resonators with multiple resonant frequencies.

B. Output DC Current Performance

By changing the load resistance from 50 Ω to 250 Ω with a step of around 25 Ω, the output dc current of the IPT system with different transfer distances is provided in Fig. 26. To evaluate the output current characteristics, an output current fluctuation rate α is introduced as

$$\alpha = \frac{I_{\text{outmax}} - I_{\text{outmin}}}{I_{\text{outmax}}} \tag{22}$$

where I_{outmax} and I_{outmin} are the maximum and minimum output dc current of the IPT system within the investigated load range. Fig. 26 exhibits that the IPT systems with transfer distances of 10 cm and 12 cm have current fluctuation rates of 18.2% and 26.2%, respectively. The parasitic resistance is the main reason for the fluctuation, and one minor reason is the slight detuning of the system for ZVS operations. The current fluctuation of the IPT system with a transfer distance of 10 cm is less than that of the case at 12 cm, which indicates a stronger coupling condition of the PCB couplers can suppress the output current variations.

C. Output Power and Efficiency Performance

The output power of the IPT system with the transfer distances of 10 cm and 12 cm at different load conditions is measured, as shown in Fig. 27. Obviously, the output power increases when the load resistance is increased for both transfer distances. With the same load condition, the output power of the IPT system with a weaker coupling condition can be higher. The corresponding overall dc–dc system efficiencies are provided in Fig. 28. For the IPT system with a transfer distance of 12 cm, the efficiency ranges from 67.09% to 89.12%. For the IPT system with a transfer distance of 10 cm, the efficiency ranges from 74.54% to 90.5%. With the same power condition, the efficiency of the IPT system with a stronger coupling condition can be higher.

D. Misalignment Tolerance

With lateral misalignment ranging from 0 to 100 mm, the coupling coefficient k at transfer distances of 100 mm and

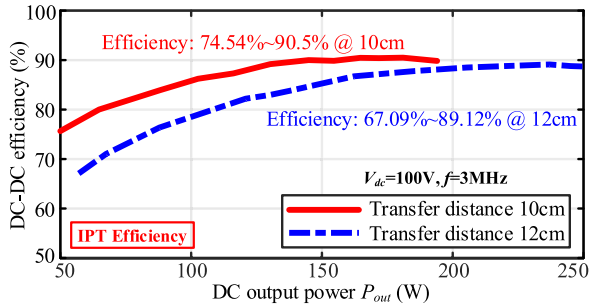

Fig. 28. Overall efficiencies of the IPT systems with different output power and transfer distances.

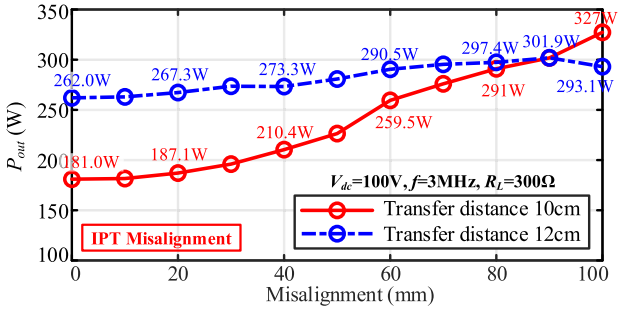

Fig. 29. Output power of the IPT systems with different misalignment conditions and transfer distances.

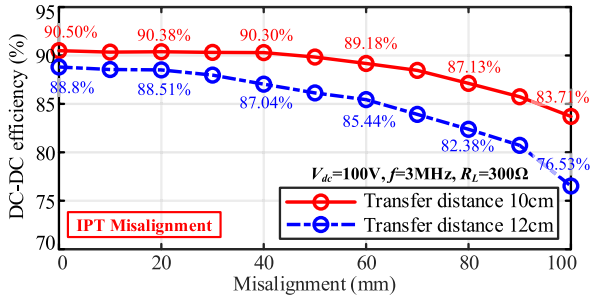

Fig. 30. Overall efficiencies of the IPT systems with different misalignment conditions and transfer distances.

120 mm ranges from 0.103 to 0.041 and from 0.075 to 0.034, respectively. The output power and efficiency of the IPT system are measured with a fixed load resistance of 300 Ω, as depicted in Figs. 29 and 30, respectively.

It shows that the output power increases with the misalignment from 262 W to 301.9 W at a transfer distance of 12 cm, while it is enhanced from 181 W to 327 W at a transfer distance of 10 cm. The system efficiencies drop from 88.8% to 76.53% for the transfer distance of 12 cm and from 90.5% to 83.7% for the transfer distance of 10 cm.

With a longer transfer distance, most of the increased system power is consumed by the parasitic resistance, contributing to a more stable output power in the case of 12 cm than that of 10 cm. Particularly, with a misalignment within 40 mm, output power at distances of 10 cm and 12 cm are only slightly increased by 29.4 W and 11 W, respectively. The corresponding dc–dc efficiencies are still over 90% and 87%.

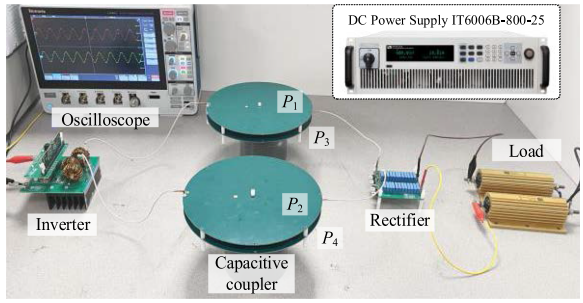

Fig. 31. Photograph of the practical CPT setup.

TABLE III
MAIN PARAMETERS OF COMPONENTS IN THE CPT SYSTEM

Parameter	Value
V_{dc}	100 V (dc)
R	300 Ω–1200 Ω
GaN FET	GS66508T
Diode	C4D02120A
Transfer distance	6 mm/15 mm/37 mm
f_s	3.015 MHz/4.610 MHz/6.78 MHz
L_r	6.7 μH/3.2 μH/1.4 μH
f_p	5.26MHz/7.67 MHz/10.63 MHz
C_s	47.6 pF/24.0 pF/16.48 pF
C_p	23.3 pF/13.5 pF/11.48 pF
L	39.3 μH/31.75 μH/19.52 μH
r	2.308Ω/2.529Ω/3.605Ω
L_m	58.53 μH/49.71 μH/32.91 μH
r_m	5.11 Ω/6.199 Ω/10.245 Ω
Misalignment	0 mm–30 mm

V. EXPERIMENTAL VERIFICATION OF PCB-BASED CPT

The photograph of the implemented 300 W CPT setup is shown in Fig. 31. The major components used in the CPT setup are similar to those used in the IPT setup. The CPT system is evaluated by load variations from 300 Ω to 1200 Ω with a misalignment range from 0 mm to 30 mm at the transfer distances of 6 mm, 15 mm, and 37 mm, respectively. The corresponding switching frequencies of the inverter (same half-bridge current source topology in IPT) are tuned at 3.125 MHz, 4.68 MHz, and 6.78 MHz, which are slightly larger than the theoretical self-resonant frequency f_s to guarantee ZVS of power switches. The detailed system parameters are provided in Table III.

A. Voltage and Current Waveforms of the Coupled Resonators

Fig. 32 exhibits the waveforms of input and output voltages and currents of the PCB resonators in the CPT system at 6 mm, 15 mm, and 37 mm and the corresponding resonant frequencies of 3.125 MHz, 4.68 MHz, and 6.78 MHz with a load resistance of 300 Ω. ZVS can be achieved in all three cases, including the case operating at 6.78 MHz shown in Fig. 32(c).

B. Output DC Voltage Performance

The output dc voltages of the CPT systems with different load conditions and transfer distances are shown in Fig. 33. The input

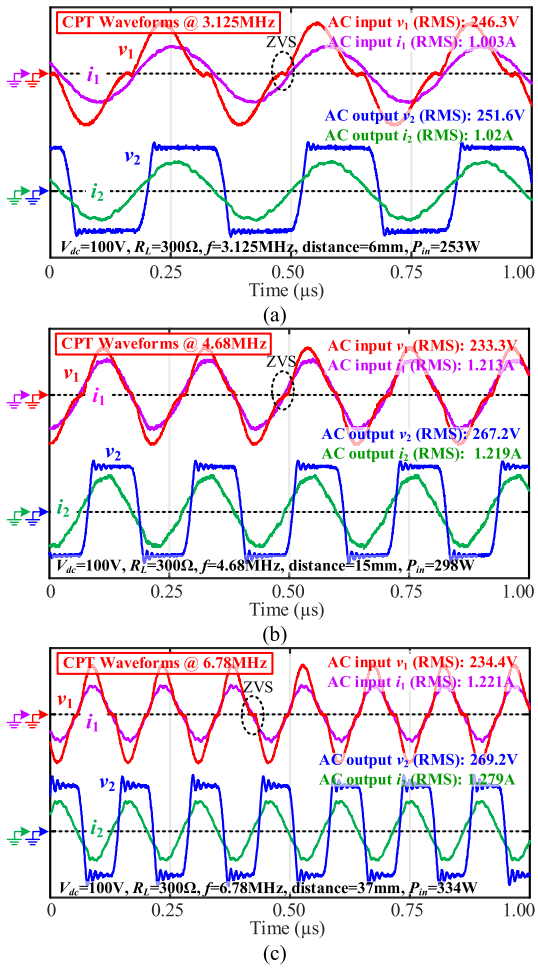

Fig. 32. Working waveforms of the CPT systems with transfer distances of (a) 6 mm (3.125 MHz), (b) 15 mm (4.68 MHz), and (c) 37 mm (6.78 MHz).

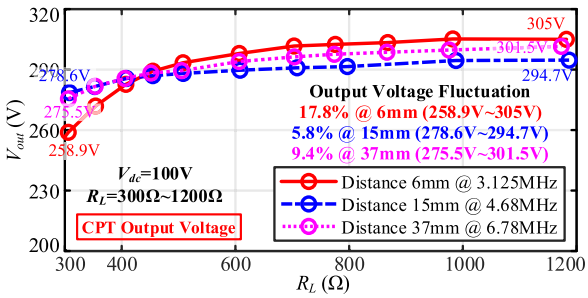

Fig. 33. Output DC voltages of the CPT systems with different load conditions and transfer distances.

dc voltages of the CPT systems are 100 V. The load resistances of the CPT systems are changed from 300 Ω to 1200 Ω. The transfer distances are set at 6 mm, 15 mm, and 37 mm. The corresponding resonant frequencies are 3.125 MHz, 4.68 MHz, and 6.78 MHz, respectively. The waveforms show the output dc voltages have 17.8%, 5.8%, and 9.4% fluctuations, which are inducted by the parasitic resistances and slight system detuning for achieving ZVS over a wide load range. The CPT system with the transfer distance of 6 mm (3.125 MHz) has the largest

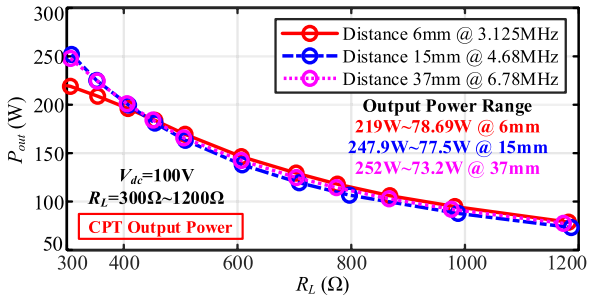

Fig. 34. Output power of the CPT systems with different load conditions and transfer distances.

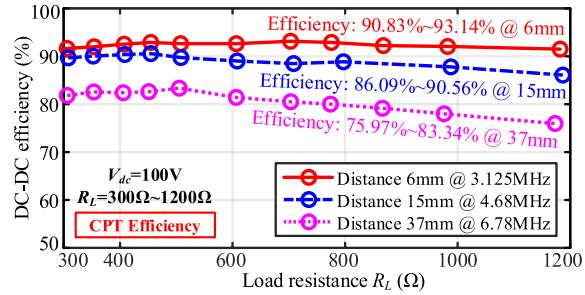

Fig. 35. Overall efficiencies of the CPT systems with different output power and transfer distances.

detuning among the three (as can be seen from Fig. 32), which results in the highest output voltage fluctuations.

C. Output Power and Efficiency Performance

The output power and overall efficiency of the CPT systems with different load conditions and transfer distances are shown in Figs. 34 and 35, respectively. It shows that the output power of CPT systems in different cases exhibits high consistencies and reduces as the load resistance increases. The CPT system with a shorter transfer distance can have a higher overall (dc–dc) efficiency. The load resistance will also affect the system efficiency. By increasing the load resistance, the system efficiency slightly increases before it drops. This is caused by the reduction of loss portions on parasitic resistances and the increase of loss portions on rectifier diodes. The maximum overall efficiencies of the CPT systems with the transfer distances of 6 mm, 15 mm, and 37 mm are 93.14%, 90.56%, and 83.34%, respectively.

D. Misalignment Tolerance

Self-resonant frequencies of the CPT systems are dependent on the coupling capacitances between the two PCBs. Thus, misalignment of coupled PCBs in the CPT systems can result in detuned operating conditions and weak power transfer capability. The output power and efficiencies of the CPT systems are illustrated in Figs. 36 and 37, respectively, considering lateral misalignments ranging from 0 mm to 30 mm, while maintaining the load resistance at 300 Ω.

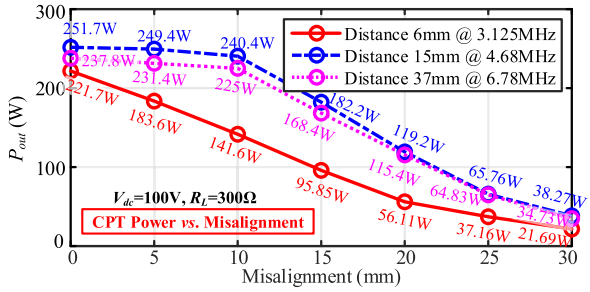

Fig. 36. Output power of the CPT systems with different misalignment conditions and transfer distances.

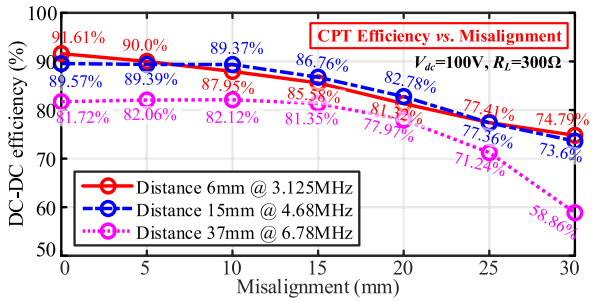

Fig. 37. Overall efficiencies of the CPT systems with different misalignment conditions and transfer distances.

For the CPT system with a transfer distance of 6 mm, the output power of the system is highly sensitive to lateral misalignment. The output power is reduced from 221.7 W to 21.69 W when the misalignment is changed from 0 mm to 30 mm. The other two CPT systems have less sensitivity to the misalignments. The output power of the CPT systems with the transfer distances of 15 mm and 37 mm slightly deviated from 251.7 W to 240.4 W and 237.8 W to 225 W for the misalignments changing from 0 mm to 10 mm, while significantly reduced to 38.27 W and 34.73 W from misalignment of 10 mm to 30 mm.

The corresponding overall (dc–dc) efficiencies are shown in Fig. 37. The efficiencies are slightly changed within the misalignment from 0 mm to 10 mm, while heavily decreased from 10 mm to 30 mm. For the CPT systems with the maximum misalignment of 30 mm, the overall system efficiencies with the transfer distances of 6 mm, 15 mm, and 37 mm are 74.79%, 73.6%, and 58.86%, respectively.

E. Comparisons Between Implemented IPT and CPT Systems

According to the analysis and experimental results, comparisons between the PCB-based IPT and CPT systems are summarized in Table IV. Ideal IPT and CPT systems exhibit load-independent CC and CV output properties. The operating frequency of an IPT system is independent of the transfer distance and misalignment, while the operating frequency of a CPT system is affected by the transfer distance and misalignments. Therefore, the CPT system has a much worse antimisalignment performance than the IPT system. However, the CPT systems perform better in antiload-variations than the IPT systems. The phase angles of the input impedances of IPT systems are changed with load variations. Hence, ZPA cannot be maintained over a wide load range for IPT systems.

TABLE IV
COMPARISONS BETWEEN THE PCB-BASED IPT AND CPT SYSTEMS

Property	IPT	CPT
Output property	CC	CV
Operating frequency	Distance-independent	Distance-dependent
Detuning in misalignment	No	Yes
Anti-misalignment	Good	Poor
ZPA at wide load range	Load-dependent	Load-independent
Anti-load-variation	Poor	Good
Preferred distance	Long	Short
Preferred condition	No load variations	No misalignment

VI. COMPARISON WITH EXISTING WORKS

The first hybrid WPT system featuring an integrated self-resonant coupler capable of simultaneous IPT and CPT might be introduced in [22]. However, its efficiency may fall short of expectations. In [23] and [24], state-of-the-art self-resonant IPT systems utilizing parallel and series self-resonators are presented. These resonators are designed for minimum parasitic resistance, resulting in high Q factors and efficiencies, albeit at elevated manufacturing costs. The resonators discussed in [26] and [30] employ copper traces on both sides of the dielectric board, which leads to a fixed self-resonant frequency. Similar issues are also observed in the works of [23] and [24]. A new PCB self-resonator with a tunable self-resonant frequency achieved by adjusting the air gap is presented in [32]. However, the demonstrated WPT performance was deemed unsatisfactory, and there was insufficient analysis of the underlying operating principles. Building upon the ideas presented in [32], this article comprehensively investigates the operating principles and efficiency performance of IPT systems utilizing improved PCB resonators. The Q factors of PCB resonators are significantly enhanced by incorporating PTFE materials. Furthermore, the implemented IPT system achieves a much higher power output with a high dc–dc efficiency over a distance of 100 mm. This represents a new performance benchmark for PCB-based self-resonant IPT systems.

This article introduces the concept of a self-resonant CPT system for the first time. Wang et al. [18] and Xia et al. [35] showcased high-performance CPT systems with significant output power and impressive efficiencies. These achievements are attributed to high-order compensation networks and high-Q components such as Litz-wire based air-core inductors and radio-frequency resonant capacitors, albeit at the cost of increased system complexity and volume.

Compared to the previous works in [22], [36], and [37], the implemented self-resonant CPT system in this article could achieve higher efficiency with a smaller coupler over similar transfer distances. Although, Sinha et al. [38] demonstrated a high transfer efficiency, the resonator requires 12 inductors and 6 capacitors for external compensation, which compromises system compactness. Overall, this article marks the first use of

PCB-based self-resonators for CPT in high-frequency applications. The resonators in the CPT system offer tunable resonant frequencies via adjustments of air gaps between PCBs, facilitating high integration without the need for external compensation components. These advancements enhance the practical applicability of CPT technology.

VII. Conclusion

In this article, integrated PCB-based self-resonators are employed to implement multi-MHz IPT and CPT systems. The IPT system achieves stable output current across a wide load variation, operating at 300 W and 3 MHz, with a maximum efficiency of 90.5% over a 10 cm distance. Similarly, utilizing the same PCB self-resonators, CPT systems at 300 W are established with operating frequencies of 3.125 MHz, 4.68 MHz, and 6.78 MHz, achieving maximum efficiencies of 93.14%, 90.56%, and 83.34% over distances of 6 mm, 15 mm, and 37 mm, respectively. Experimental findings indicate that the implemented self-resonant IPT systems demonstrate superior performance against misalignment compared to the self-resonant CPT systems, while the CPT systems exhibit better resilience against load variation. Moreover, PCB-based self-resonators are deemed more suitable for IPT mode in scenarios involving longer transfer distances and minimal load variations. Conversely, for shorter distances with slight misalignment, operating in CPT mode is recommended.

References

[1] G. Covic and J. T. Boys, "Inductive power transfer," *Proc. IEEE*, vol. 101, no. 6, pp. 1276–1289, Jun. 2013.

[2] S. Y. R. Hui, "Planar wireless charging technology for portable electronic products and Qi," *Proc. IEEE*, vol. 101, no. 6, pp. 1290–1301, Jun. 2013.

[3] C. T. Rim and C. Mi, *Wireless Power Transfer*. New York, NY, USA: Wiley, 2017.

[4] Y.-G. Su, S.-Y. Xie, A. P. Hu, C.-S. Tang, W. Zhou, and L. Huang, "Capacitive power transfer system with a mixed-resonant topology for constant-current multiple-pickup applications," *IEEE Trans. Power Electron.*, vol. 32, no. 11, pp. 8778–8786, Nov. 2017.

[5] "Qi Specification," [Online]. Available: https://www.wirelesspowerconsortium.com/knowledge-base/specifications/download-the-qi-specifications/

[6] J. Dai and D. C. Ludois, "A survey of wireless power transfer and a critical comparison of inductive and capacitive coupling for small gap applications," *IEEE Trans. Power Electron.*, vol. 30, no. 11, pp. 6017–6029, Nov. 2015.

[7] C. Qi, G. Zheng, Y. Liu, J. Liang, H. Wang, and M. Fu, "A simplified three-order small-signal model for capacitive power transfer system using series compensation," *IEEE Trans. Power Electron.*, vol. 38, no. 5, pp. 5688–5692, May 2023.

[8] Y. Wang, H. Zhang, and F. Lu, "Review, analysis, and design of four basic CPT topologies and the application of high-order compensation networks," *IEEE Trans. Power Electron*, vol. 37, no. 5, pp. 6181–6193, May 2022.

[9] S. Yao et al., "Coupler comparison of inductive and capacitive power transfer systems," in *Proc. 2022 Int. Conf. Wireless Power Transfer*, 2022, pp. 523–530.

[10] Y. Wang, H. Zhang, Y. Cao, and F. Lu, "Remaining opportunities in capacitive power transfer based on duality with inductive power transfer," *IEEE Trans. Transp. Electrif.*, vol. 9, no. 2, pp. 2902–2915, Jun. 2023.

[11] X. Dai, M. Sun, P. Deng, R. Wang, and Y. Su, "Asymmetric bidirectional capacitive power transfer method with push-pull full-bridge hybrid topology," *IEEE Trans. Power Electron.*, vol. 37, no. 11, pp. 13902–13913, Nov. 2022.

[12] W. Gu, D. Qiu, X. Shu, B. Zhang, W. Xiao, and Y. Chen, "A constant output capacitive wireless power transfer system based on parity-time symmetric," *IEEE Trans. Circuits Syst. II, Exp. Briefs*, vol. 70, no. 7, pp. 2585–2589, Jul. 2023.

[13] E. Culurciello and A. G. Andreou, "Capacitive inter-chip data and power transfer for 3-D VLSI," *IEEE Trans. Circuits Syst. II, Exp. Briefs*, vol. 53, no. 12, pp. 1348–1352, Dec. 2006.

[14] A. P. Hu, C. Liu, and H. L. Li, "A novel contactless battery charging system for soccer playing robot," in *Proc. 2008 15th Int. Conf. Mechatronics Mach. Vis. Pract.*, Auckland, New Zealand, 2008, pp. 646–650.

[15] D. C. Ludois, J. K. Reed, and K. Hanson, "Capacitive power transfer for rotor field current in synchronous machines," *IEEE Trans. Power Electron.*, vol. 27, no. 11, pp. 4638–4645, Nov. 2012.

[16] F. Lu, H. Zhang, H. Hofmann, and C. Mi, "A double-sided LCLC-compensated capacitive power transfer system for electric vehicle charging," *IEEE Trans. Power Electron.*, vol. 30, no. 11, pp. 6011–6014, Nov. 2015.

[17] B. Luo, A. P. Hu, H. Munir, Q. Zhu, R. Mai, and Z. He, "Compensation network design of CPT systems for achieving maximum power transfer under coupling voltage constraints," *IEEE J. Emerg. Sel. Topics Power Electron.*, vol. 10, no. 1, pp. 138–148, Feb. 2022.

[18] Y. Wang, H. Zhang, and F. Lu, "3.5-kW 94.2% DC–DC efficiency capacitive power transfer with zero reactive power circulating," *IEEE Trans. Power Electron.*, vol. 38, no. 2, pp. 1479–1484, Feb. 2023.

[19] B. Regensburger, S. Sinha, A. Kumar, S. Maji, and K. K. Afridi, "High-performance multi-MHz capacitive wireless power transfer system for EV charging utilizing interleaved foil coupled inductors," *IEEE J. Emerg. Sel. Topics Power Electron.*, vol. 10, no. 1, pp. 35–51, Feb. 2022.

[20] S. Y. R. Hui, Y. Yang, and C. Zhang, "Wireless power transfer: A paradigm shift for the next generation," *IEEE J. Emerg. Sel. Topics Power Electron.*, vol. 11, no. 3, pp. 2412–2427, Jun. 2023.

[21] D. Vincent, P. S. Huynh, N. A. Azeez, L. Patnaik, and S. S. Williamson, "Evolution of hybrid inductive and capacitive AC links for wireless EV charging—A comparative overview," *IEEE Trans. Transp. Electrific.*, vol. 5, no. 4, pp. 1060–1077, Dec. 2019.

[22] F. Lu, H. Zhang, H. Hofmann, and C. Mi, "An inductive and capacitive integrated coupler and its LCL compensation circuit design for wireless power transfer," *IEEE Trans. Ind. Appl.*, vol. 53, no. 5, pp. 4903–4913, Sep./Oct. 2017.

[23] L. Gu, G. Zulauf, A. Stein, P. A. Kyaw, T. Chen, and J. M. R. Davila, "6.78-MHz wireless power transfer with self-resonant coils at 95% DC–DC efficiency," *IEEE Trans. Power Electron.*, vol. 36, no. 3, pp. 2456–2460, Mar. 2021.

[24] R. Qin, J. Li, and D. Costinett, "A 6.6-kW high-frequency wireless power transfer system for electric vehicle charging using multilayer nonuniform self-resonant coil at MHz," *IEEE Trans. Power Electron.*, vol. 37, no. 4, pp. 4842–4856, Apr. 2022.

[25] A. L. F. Stein, P. A. Kyaw, and C. R. Sullivan, "Wireless power transfer utilizing a high-Q self-resonant structure," *IEEE Tran. Power Electron.*, vol. 34, no. 7, pp. 6722–6735, Jul. 2019.

[26] Z. Yi, M. Li, B. Muneer, G. He, and X.-X. Yang, "Self-resonant antisymmetric planar coil for compact inductive power transfer system avoiding compensation circuits," *IEEE Trans. Power Electron.*, vol. 36, no. 5, pp. 5121–5134, May 2021.

[27] J. Li and D. Costinett, "Analysis and design of a series self-resonant coil for wireless power transfer," in *Proc. 2018 IEEE Appl. Power Electron. Conf. Expo.*, San Antonio, TX, USA, 2018, pp. 1052–1059.

[28] K. Li, J. Wu, M. Wang, A. C. Yucel, and S.-Y. R. Hui, "A sandwich structure for cost-effective printed-circuit-board wireless power resonator," in *Proc 2023 IEEE Appl. Power Electron. Conf. Expo.*, Orlando, FL, USA, 2023, pp. 818–821.

[29] K. Chen and Z. Zhao, "Analysis of the double-layer printed spiral coil for wireless power transfer," *IEEE J. Emerg. Sel. Topics Power Electron.*, vol. 1, no. 2, pp. 114–121, Jun. 2013.

[30] Y. Fang, J. Qu, B. M. H. Pong, C. K. Lee, and R. S. Y. Hui, "Quasi-static modeling and optimization of two-layer PCB resonators in wireless power transfer systems for 110-kV power grid online monitoring equipment," *IEEE Trans. Ind. Electron.*, vol. 69, no. 2, pp. 1400–1410, Feb. 2022.

[31] J. Qu, L. He, N. Tang, and C.-K. Lee, "Wireless power transfer using domino-resonator for 110-kV power grid online monitoring equipment," *IEEE Trans. Power Electron.*, vol. 35, no. 11, pp. 11380–11390, Nov. 2020.

[32] K. Li, J. Wu, A. C. Yucel, and S.-Y. R. Hui, "New printed-circuit-board resonators with high quality factor and transmission efficiency for megahertz wireless power transfer applications," *IEEE Trans. Power Electron.*, vol. 38, no. 10, pp. 13207–13218, Oct. 2023.

[33] M. Fu, Z. Tang, and C. Ma, "Analysis and optimized design of compensation capacitors for a megahertz WPT system using full-bridge rectifier," *IEEE Trans. Ind. Inform.*, vol. 15, no. 1, pp. 95–104, Jan. 2019.

[34] Y. Yang, "Precise modeling of nonlinear rectifier loads in wireless power transfer systems," *IEEE J. Emerg. Sel. Topics Power Electron.*, vol. 11, no. 3, pp. 3574–3585, Jun. 2023.
[35] J. Xia, X. Yuan, S. Lu, J. Li, S. Luo, and S. Li, "A two-stage parameter optimization method for capacitive power transfer systems," *IEEE Trans. Power Electron.*, vol. 37, no. 1, pp. 1102–1117, Jan. 2022.
[36] H. Zhang and F. Lu, "An improved design methodology of the double-sided LC-compensated CPT system considering the inductance detuning," *IEEE Trans. Power Electron.*, vol. 34, no. 11, pp. 11396–11406, Nov. 2019.
[37] X. Wu, Y. Su, A. P. Hu, X. Qing, and X. Hou, "Multiobjective parameter optimization of a four-plate capacitive power transfer system," *IEEE J. Emerg. Sel. Topics Power Electron.*, vol. 9, no. 2, pp. 2328–2342, Apr. 2021.
[38] S. Sinha, A. Kumar, B. Regensburger, and K. K. Afridi, "Design of high-efficiency matching networks for capacitive wireless power transfer systems," *IEEE J. Emerg. Sel. Topics Power Electron.*, vol. 10, no. 1, pp. 104–127, Feb. 2022.

Yao Wang (Member, IEEE) received the bachelor's and master's degrees from Northwestern Polytechnical University, Xi'an, China, in 2017 and 2020, respectively, and the Doctorate degree from Drexel University, Philadelphia, PA, USA, in 2023, all in electrical engineering.

He is currently a Postdoctoral Research Fellow with Nanyang Technological University, Singapore. His research interests include high-power capacitive power transfer, inductive electric vehicle charging, high-frequency power conversion, and wide bandgap device applications.

Kaiyuan Wang (Student Member, IEEE) received the B.Eng. degree from Northeast Electric Power University, Jilin City, China, in 2020, and the M.Sc. degree from The University of Hong Kong, Hong Kong, in 2021, and the M.Phil. degree from The Hong Kong Polytechnic University, Hong Kong, in 2023. He is currently working toward the Ph.D. degree with Nanyang Technological University, Singapore, all in electrical engineering.

His research interests include wireless power transfer and power electronics.

Dr. Wang is a best paper award recipient of the 12th APSCOM2022.

Kerui Li (Member, IEEE) received the B.Eng. degree in integrated circuit design and system integration from the South China University of Technology, Guangzhou, China, in 2013, the M.Eng. degree in information and communications engineering from the Sun Yat-sen University, Guangzhou, China, in 2016, and the Ph.D. degree in electrical and electronic engineering from The University of Hong Kong, Hong Kong, in 2021.

He is currently a Research Assistant Professor with the Department of Electrical and Electronic Engineering, The University of Hong Kong. Prior to that, he was a Research Fellow with Nanyang Technological University and a Research Assistant Professor with The Hong Kong Polytechnic University. His research interests include power electronics and wireless power transfer.

Dr. Li was the recipient of IEEE TRANSACTIONS ON POWER ELECTRONICS Prize Paper Award (First Place) in 2023, the IEEE Power Electronics Society Ph.D. Thesis Talk Award in 2022, and The University of Hong Kong Power Engineering Prize in 2020.

Yun Yang (Senior Member, IEEE) received the B.Sc. degree from Wuhan University, Wuhan, China, in 2012, and the Ph.D. degree from The University of Hong Kong, Hong Kong, in 2017, both in electrical engineering.

He was a Research Assistant Professor with the Department of Electrical Engineering, The Hong Kong Polytechnic University. He is currently an Assistant Professor with the School of Electrical and Electronic Engineering, Nanyang Technological University. His research interests include wireless power transfer, renewable energy technologies, electric vehicles, power electronics, and advanced control.

Shu Yuen Ron Hui (Fellow, IEEE) received the B.Sc. (Eng.; hons.) degree in electrical and electronic engineering from the University of Birmingham, Birmingham, U.K., in 1984, and the D.I.C. and Ph.D. degrees in electrical engineering from Imperial College London, London, U.K., in 1987.

He is a Philip Wong Wilson Wong Professor with the University of Hong Kong and a Chair Professorship of Power Electronics with Imperial College London. He held the MediaTek Endowed Professorship with Nanyang Technological University. He has authored or coauthored more than 500 research papers, including 300 refereed journal publications. More than 120 of his patents have been adopted by industry worldwide. His inventions on wireless charging platform technology underpin key dimensions of Qi, the world's first wireless power standard, with freedom of positioning and localized charging features for wireless charging of consumer electronics. He has also developed the photo-electro-thermal theory for LED systems and electric spring technology for smart grid. His research interests include power electronics, wireless power, sustainable lighting, and smart grid.

Dr. Hui was the recipient of the IEEE Rudolf Chope R&D Award and the IET Achievement Medal (The Crompton Medal) in 2010, and IEEE William E. Newell Power Electronics Award in 2015. He is a Fellow of the Australian Academy of Technological Sciences and Engineering, US National Academy of Inventors, and Royal Academy of Engineering, U.K.